

Comparison between different non-destructive techniques methods to detect and characterize impact damage on composite laminates

I Papa^{1,*} , MR Ricciardi^{2,*}, V Antonucci² , A Langella¹, J Tirillò³, F Sarasini³, V Pagliarulo⁴, P Ferraro⁴ and V Lopresto¹

Journal of Composite Materials
2020, Vol. 54(5) 617–631
© The Author(s) 2019
Article reuse guidelines:
sagepub.com/journals-permissions
DOI: 10.1177/0021998319864411
journals.sagepub.com/home/jcm



Abstract

This paper aims to investigate the ability of ultrasonic and electronic speckle pattern interferometry to analyse the low-velocity impact internal damage mechanisms on basalt composite laminates and to provide information on the shape and the extent of the delamination in non-destructive way.

Basalt/epoxy composites with different thicknesses have been realised and characterised by mechanical tests to investigate both fibre-dominated (tensile and flexural behaviour) and matrix-dominated properties (interlaminar shear strength). Specimens were impacted at penetration and at increasing energy values, to explore the damage onset and propagation. The results showed that the damage was concentrated under the impactor–material contact point and that the composite with intermediate thickness had the best balance between the different kinds of impact damages: delamination and indentation. Further, a good agreement was found between the overall data obtained by the two non-destructive techniques, confirming the capability of both techniques to examine the composite impact damage.

Keywords

Basalt laminates, low-velocity impact, delamination, ultrasonic, electronic speckle pattern interferometry

Introduction

Recently, basalt fibre laminates have been extensively investigated for potential applications in civil, naval and automotive fields.¹ The main reason has to be found in the increasing interest in the environment that has promoted the use of natural fibres as reinforcement in polymer matrices.² The use of basalt fibres is supported by the large availability and the manufacturing process similar to that of glass fibres, but without the need of any precursor nor additive, thus leading to a global reduction of the environmental impact.

Basalt fibres exhibit excellent sound insulation properties, excellent heat resistance, good chemical resistance and low water absorption that, coupled with mechanical properties comparable to those of glass fibres, make these fibres attractive to potentially replace the latter in industrial fields like aerospace, automotive, transportation and shipbuilding.^{1,3–5} In spite of basalt fibres availability, their use as reinforcement in polymer

matrices is a relatively new application that could offer very interesting and environmental perspectives,^{3,6–9} also because the size of the fibre diameters, usually higher than 6 μm, does not induce risk of toxicity, according to European law (97/69/Ce and 1907/2006). Further, in the field of composite materials, basalt fibres have already shown some potential regarding

¹Department of Chemical, Materials and Production Engineering, University of Naples Federico II, Italy

²Institute for Polymer, Composites and biomaterials, National Research Council, Italy

³Department of Chemical Engineering Materials Environment, Sapienza University of Rome, Italy

⁴National Council of Research – Institute of Applied Sciences & Intelligent Systems (ISASI), Italy

*These authors contributed equally to this work.

Corresponding author:

V Antonucci, CNR P.le Enrico Fermi, I Portici, Napoli 80055, Italy.
Email: vinanton@unina.it

energy absorption, as detailed in Lopresto et al.³ and Sarasini et al.¹⁰ In Lopresto et al.,³ low-velocity impact tests were performed at about 100 J to perforate the composite specimens, and the results showed a higher energy absorption capability for basalt in comparison to glass fibre-reinforced composites. Over the years, several studies on the low-velocity impact response of basalt laminates have been proposed, even considering their use in hybrid structures.^{10–12} However, a detailed analysis of the influence of the laminate thickness on the onset and the development of impact damage still deserves attention,¹³ as this parameter is known to significantly affect the maximum force, the energy at maximum force and penetration energy. Evaluation and quantification of impact damage extension are critical, as during an impact event delamination is observed to be a significant failure mode, which can severely compromise the post-impact mechanical performance of the composite structure. Ultrasonic C-scan is commonly used to detect defects induced during fabrication and damage resulting from in-service conditions,¹⁴ but other less conventional inspection methods based on holography have been proposed over the years and demonstrated great potential in revealing delaminations in composites.^{15,16} These techniques, based on the ability of holographic interferometry to measure out-of-plane displacements with high sensitivity, show several advantages, including their non-contact nature, thus making it possible to carry out full-field analyses on the surface of components with complex geometry. Among these, a method based on speckle interferometry, the electronic speckle pattern interferometry (ESPI),¹⁷ has been already applied for damage detection in composite laminates with the advantage of showing fringe patterns in real time, thus speeding up the testing procedure, even if issues related to its low signal-to-noise ratio have been raised in the past.¹⁸ Recently, this technique proved to be useful for investigating impact damage induced in basalt/flax hybrid composites,¹⁹ while a direct comparison with a standard Ultrasonic C-scan technique has never been proposed for basalt laminates.

In this framework, basalt fibre-reinforced epoxy laminates were realised by stacking plain woven fabrics that were impregnated by vacuum resin infusion. The basalt/epoxy composites have been characterised by quasi-static mechanical tests to investigate tensile and flexural behaviour and interlaminar shear strength (ILSS) as a function of laminate thickness. Also, low-velocity impact tests have been carried out at increasing energy values up to penetration, to investigate the damage onset and propagation. Two different non-destructive techniques (NDTs), Ultrasonic C-scan and ESPI, were used to estimate the internal damage and to offer valid alternative methods for the non-visible damage assessment.

Experimental

Materials

Basalt fibre-reinforced plastic square laminates, 400 mm × 400 mm, were realised by resin vacuum infusion technology⁵ using basalt plain woven fabrics, 200 g/m² (Basaltex NV) and an epoxy infusion system by Gurit (Prime 20LV). Fabric layers of 16, 22 and 30 were stacked between one-sided rigid mould and a formable vacuum bag material to obtain different target thicknesses, ranging from 2.50 to 5.00 mm, investigate the effect of this parameter on the quasi-static and impulsive properties. The fibres were impregnated by injecting the resin from an input channel. Vacuum at 0.85 bar was applied through multiple vents in order to remove the air from the fibre preform and to drive the fibre impregnation by resin. A resin distribution net medium was placed onto the reinforcement to promote the resin flow allowing the complete wet-out of the preform and eliminating voids and dry spots. After infusion, the panels were cured for 16 h at 50°C.

Testing techniques

Density and constituent content tests. Density and constituent content tests have been performed according to the ASTM D792 and ASTM D3171 standards, respectively. In particular, the ASTM D792 involves weighing a one-piece specimen of 1–50 g in the air and then in demineralised water, the ratio between the weight of the sample in air and the difference between the weight in air and water gives the density of the sample. On the other hand, the fibre weight content of manufactured composites has been evaluated by burning the composite samples and weighing the remaining residue. By the knowledge of composites density, the fibre volume fraction has been calculated by the following relationship (equation (1))

$$V_r = \frac{M_f}{M_i} * 100 * \frac{\rho_c}{\rho_r} \quad (1)$$

where M_i is the initial mass of the sample, M_f is the final mass of the sample after burning, ρ_c is the sample density and ρ_r is the density of the reinforcement. Similarly, the matrix volume fraction can be calculated by equation (2)

$$V_m = \frac{(M_i - M_f)}{M_i} * \frac{\rho_c}{\rho_m} \quad (2)$$

where ρ_m is the matrix density.

Morphological analysis (SEM). The morphology of the fracture surface of the investigated composites was

studied by using a Quanta 200 FEG (FEI Company, Eindhoven, the Netherlands) scanning electron microscope (SEM). Before the investigation, samples were sputter coated with a boron palladium film (Emitech K575X).

Quasi-static mechanical properties of composite laminates.

The specimens for the mechanical characterisation were cut from the realised composite plates. Quasi-static tensile tests on prismatic samples were performed according to ASTM D 3039, using an electromechanical testing machine Instron 5584, equipped with a load cell of 150 kN. Five specimens were tested with the following dimensions 200 mm × 25 mm × 2.5 mm (L × W × t). The strain of the specimens was measured by an extensometer with sensor arms, using a gauge length of 80 mm. Tensile tests were carried out in displacement control at a crosshead speed of 2 mm/min. Four-point bending tests were performed on five prismatic samples (130 mm × 15 mm × 2.5 mm) by ASTM D 6272, by using an electromechanical testing machine Zwick/Roell Z010, equipped with a 10 kN load cell. A span-to-depth ratio of 32:1 and a crosshead speed of 2.5 mm/min were used. The ILSS was evaluated by ASTM D 2344 by using the short beam shear (SBS) method, where the interlaminar shear is indirectly generated through three-point bending. In this test, the determination of ILSS is based on Bernoulli–Euler beam theory and for a beam of rectangular cross-section loaded in three-point bending, the maximum interlaminar shear stress occurs at the mid-thickness of the beam between the centre and end supports and is calculated to be (equation (3))

$$ILSS = \frac{3P_m}{4wt} \quad (3)$$

where P_m is the maximum load and w and t are the width and the thickness of the beam, respectively. A span-to-thickness ratio of 4 was used, as recommended by the ASTM standard, while samples were compliant with the following dimensions: length = 6 × t and width = 2 × t . Tests on at least five samples were performed in displacement control at a crosshead speed of 1 mm/min using an electromechanical testing machine Zwick/Roell Z010, equipped with a 10 kN load cell.

Impact properties of composite laminates. Impact tests were carried out by a falling weight machine, Ceast Fractovis, at complete penetration, to obtain and study the whole load–displacement curve, which provides useful information about the response of the laminates. Then, different increasing energy levels corresponding to 25, 50, 75% of the increasing linear part

of the curve were chosen to carry out the so-called indentation tests, useful to study the damage onset and evolution. The rectangular specimens, 100 mm × 150 mm, cut by a diamond saw from the original panels, were supported by the clamping device suggested by the ASTM D7137 Standard and were centrally loaded by an instrumented cylindrical impactor with a hemispherical nose, 19.8 mm in diameter. A total minimum mass of 3.640 kg combined with the drop heights allowed to obtain the selected impact energies. After the impact tests, the specimens were observed by visual inspection to investigate the external damage, whereas a confocal microscope, Leica DCM3D, was used to measure the residual indentation depth.

The preceding equipment allows the acquisition of the tridimensional shape of the surface and dedicated software can measure the indentation depth. In Figure 1, an example of the image acquisition is reported: it is possible to appreciate the high resolution. The superficial imperfections resulting in roughness do not affect the measurements.

From the three-dimensional image in Figure 1, it is possible to cut the section from which the information about the profile of the same section derives and, in the case of the impacted specimens, to measure the depth of the indentation left by the indenter after the dynamic load.

In Figure 2, the typical profile obtained in correspondence of the cross-section of the indentation is reported. Once obtained the profile, it is straightforward to measure the indentation as the maximum depth with respect to the reference point.

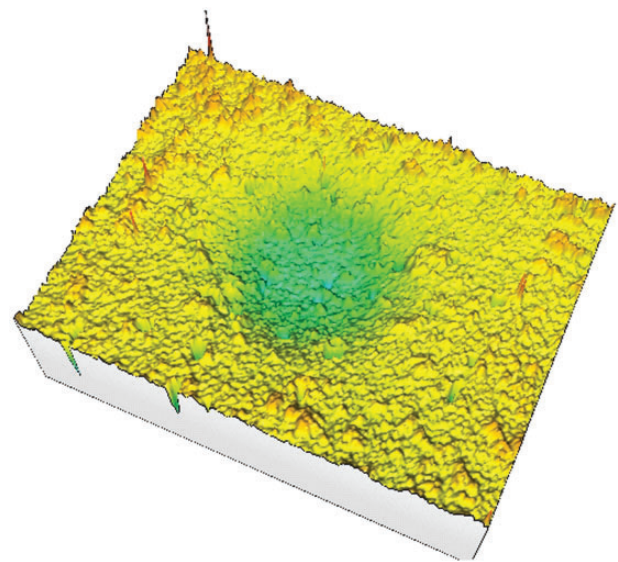


Figure 1. Example of the three-dimensional shape acquisition of the impacted sample surface.

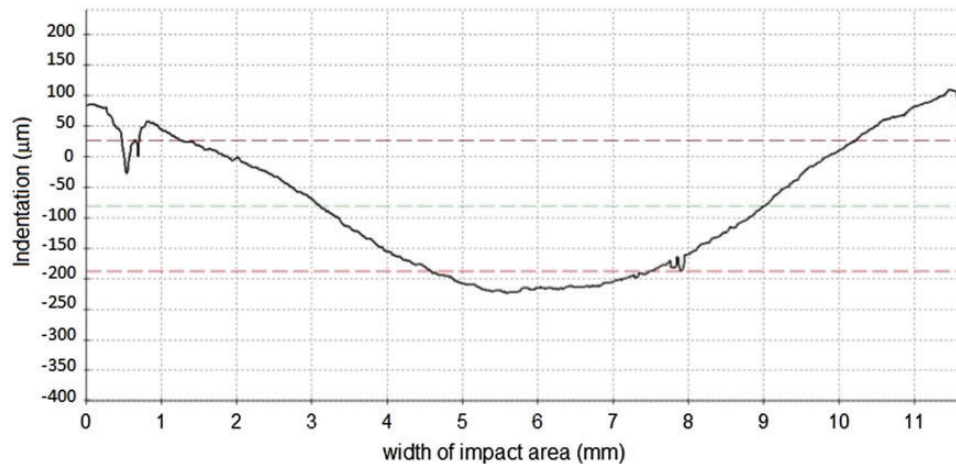


Figure 2. Example of profile obtained in correspondence of the cross section of the indentation.

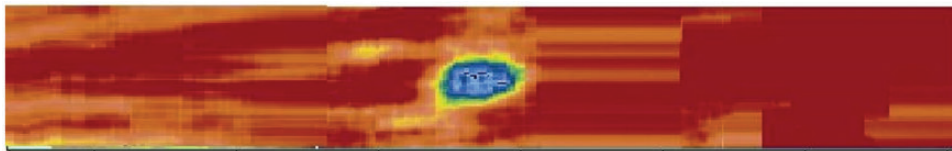


Figure 3. Example of damage detection using ultrasound scans (16 ply-U = 10J).

Non-destructive inspection of laminates. The superficial and internal damage caused by low-velocity impacts was analysed by two different NDT. Ultrasound scans were performed with a 5 MHz head (M2M Multi Pocket system, Phased Array Probe, 5 MHz Linear Array, 64 Elements).

The advantages of phased array technology, compared to conventional ultrasound, derive from the possibility to use several elements assembled in a single transducer to guide, focus and scan the beams. The orientation of the beams, generally called the sector scan, can be used to map the components at an optimum angle. In this way, it is possible to simplify the inspection of components with complex shapes. The choice of a low-frequency probe ($f = 5$ MHz) is justified by a significant decrease in the signal attenuation and a more efficient measurement.^{41,42}

The probe is used for the emission and the reception of the ultrasound waves. The pulse-echo technique²⁰ was used for the acquisition of internal damage data. The depth of a reflective structure is inferred from the delay between pulse transmission and echo reception. The correct plate thickness, using this method on an undamaged sample, is obtained, and the acquisition system is calibrated (Figure 3). The propagation velocity through the material, equal to 2600 mm/s, is calculated by Scarponi.⁴²

C-scan inspections were applied to provide a plane view of specimens subjected to ultrasound analysis, and

they were captured using ultrasonic evaluation before and after impact, providing a baseline for damage and also allowing for the identification of fabrication flaws. By appropriately setting the Gate, a more transparent image of the internal delamination was obtained. The ultrasonic (US) user can choose from a list of detection modes. The user can specify the type of detection algorithm to be used to trigger data recording in a time gate, the. One echo is defined either as a global or local extremum (maximum or minimum) of the summed signal consideration.

It is defined by a couple (amplitude, time-of-flight) also called a peak. In this work, among the different available detection options, the Echo max abs were used. This detection mode triggers data recording if the absolute (positive or negative) maximum peak detected within the gate width is above the gate threshold. The returned value is the maximum peak, and it will be recorded.

The signal is more or less attenuated when crossing the material. This depends on the absorption coefficient of the latter and the variation in its density due to the presence of obstacles (air or debris occlusions) and damage to the matrix and fibre. Depending on the height of overrun Gate (and therefore on the amplitude of the signal), a different colour is evidenced on the C-scan. Each delaminated area was, then, imported in a cad software where it was bordered and measured.

ESPI technique allows to measure the out of plane displacements of a specimen after a stress event and, in such

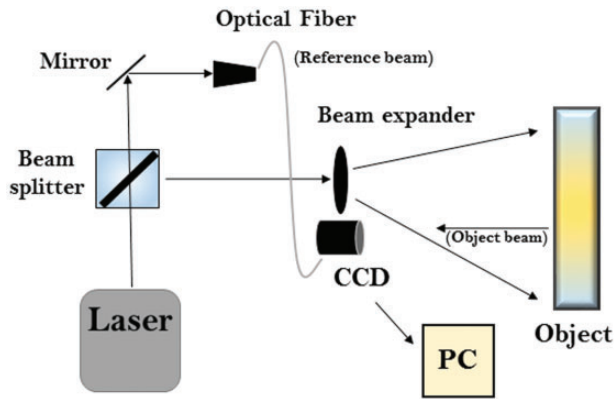


Figure 4. Optical setup of ESPI.

way, enables to identify cracks, strain and flaws on rough surfaces with high sensitivity in real-time and full-field modality without contact.^{21–23} The detection of micro-deformations is obtained illuminating the sample surface with a visible laser (wavelength of 532 nm). A Charge-Coupled Device/complementary metal-oxide semiconductor (CCD/CMOS) camera records the deformation under correlation fringes shape, deformation due to for example slight warming imposed on the material. A typical scheme of the system for recording speckle interferometry measurements is illustrated in Figure 4.

The laser beam is split into a reference beam and an object beam using a beam splitter (BS), which enables control of the relation between the reference beam and an object beam. The reference beam is coupled into an optical fibre reaching a CCD sensor where also the light scattered from the object is addressed. Before reaching the object, the object beam passes through an electronically tilted etalon to shift the probing beam laterally in a parallel direction obtaining four similar images of the speckle pattern, which are used to perform an average to reduce the speckle noise. Upon an external perturbation, the object is deformed, and the reflected wavefront is slightly changed concerning the initial state, while the reference beam remains unperturbed. Thus, after the record of a first speckle image without any perturbation, the CCD camera records a new speckle pattern, and the subtraction of the two registered speckle patterns (deformed and non-deformed states) provides the correlation fringes. The speckle pattern intensity for the unperturbed state is given by equation (4)

$$I_1 = I_0 + I_r + 2\sqrt{I_0 I_r} \cos(\theta) \quad (4)$$

while for the deformed state is given by equation 5

$$I_2 = I_0 + I_r + 2\sqrt{I_0 I_r} \cos(\theta + \phi) \quad (5)$$

where I_0 is the intensity scattered from the object, I_r is the reference beam, θ is the phase angle and ϕ is related

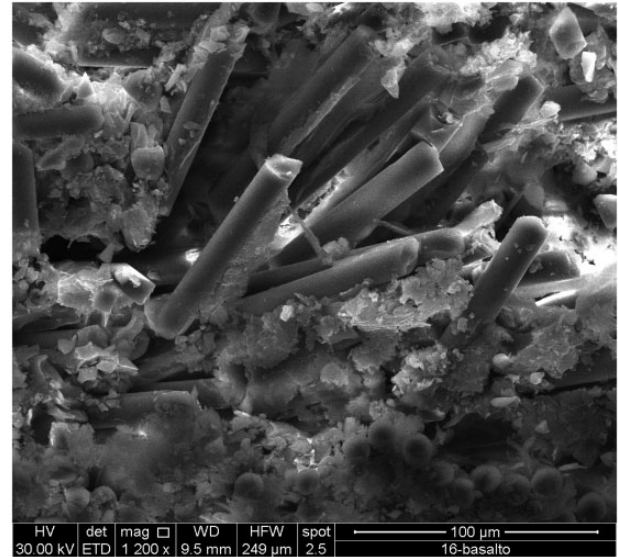


Figure 5. SEM analysis of basalt fibre–reinforced epoxy composites.

to the displacement. The fringes patterns that represent the out-of-plane surface displacement are represented by equation (6)

$$I_{1-2} = 2\sqrt{I_0 I_r} [\cos \theta - \cos(\theta + \phi)] \quad (6)$$

The correlation fringes allow obtaining the phase-contrast maps, from which it is possible to measure the displacement field quantitatively. The calculation of phase-contrast map is obtained by using well-known numerical processing, consisting into demodulation of the fringe pattern image, which provides a wrapped phase image, and the subsequent unwrapping step.²⁴

Results and discussion

The density of the basalt/epoxy composites was found to be equal to 1.87 g/cm³, while the measured fibre volume fractions of the different composites showed limited differences, resulting in 0.69 for the 16-ply and 22-ply composites and 0.68 for the 30-ply composite, demonstrating the excellent quality of the adopted manufacturing technique. In addition, the void percentage resulted below 3%.

The SEM has been used to investigate the morphology of the realised basalt composites. Figure 5 shows a SEM micrograph of a cryofractured surface of the basalt fibre/epoxy composite. A good impregnation of the fibres can be observed confirming the capability of the vacuum infusion process to produce basalt/epoxy composites with high fibre content. Furthermore, no evidence of debonding is detected, and despite the smooth surface of some basalt fibres, they appear to

Table 1. Quasi-static mechanical properties of basalt fibre-reinforced epoxy composites.

Property	Basalt/epoxy laminate
Tensile strength (MPa)	439.33 ± 9.53
Tensile modulus (GPa)	24.32 ± 0.49
Flexural strength (Mpa)	440.14 ± 27.90
Flexural modulus (GPa)	26.05 ± 2.44

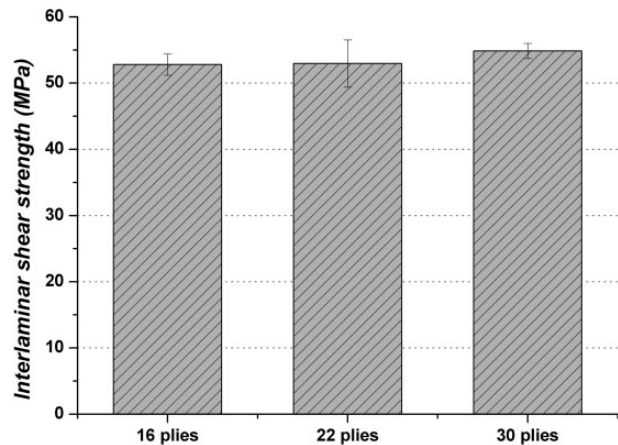
be fractured on the same plane, thus suggesting an adequate level of interfacial adhesion between basalt fibres and epoxy matrix.

Quasi-static mechanical properties

The manufactured composites were subjected to a preliminary detailed mechanical characterisation aimed to address the quality of the laminates by investigating both fibre-dominated (tensile and flexural behaviour) and matrix-dominated properties (ILSS via SBS test). In this way, it is possible to assess the degree and quality of fibre impregnation along with the fibre/matrix adhesion strength. Table 1 summarises the tensile and flexural properties of basalt fibre-reinforced composites.

As a general comment, the laminates exhibited a limited dispersion in results, thus highlighting a consistent mechanical behaviour due to a reliable manufacturing process. The resulting flexural and tensile properties compare quite favourably with those of other studies if one considers the inevitable differences in fibre-stacking sequence, matrix type and fibre volume fraction.^{3,6,25,26} During bending tests, basalt composites exhibited a mixed fracture mode, involving damage on both the compressed and tensile half sections, thus making negligible the difference in strength between the flexure and the tension test, which is a well-known consequence of the size effect: the decrease of mean strength with increasing flaw-sensitive volume under stress.

On the other hand, the ILSS is generally considered a limiting design property for composites as it can be the result of complex interactions of many parameters, including fibre/matrix adhesion, constitutive materials properties, fibre volume fraction and stacking sequence. In any case, it also represents an essential quantity for evaluating fabrication quality, especially the consolidation of composites.²⁷ This explains why a significant number of tests have been developed over the years for its accurate determination, all being designed to load the specimen so that it fails in interlaminar shear and the shear stress at failure is taken as the ILSS. In this regard, the SBS method is the simplest and,

**Figure 6.** ILSS of basalt/epoxy composites measured by short beam shear (SBS).

therefore, the most used in practice, even if it suffers from several limitations²⁸ that make this test mostly suitable for quality control purposes rather than for design. In the present study, to assess the quality of the manufactured composites regarding fibre impregnation, the ILSS values have been calculated for three different laminates characterised by increasing number of layers and thickness, but with constant overall fibre volume fraction. The results are shown in Figure 6.

The results exhibit negligible differences as a function of number of layers and thickness, thus providing an indirect confirmation of the successful manufacturing process without any filtering effect of fabrics able to prevent the resin from penetrating through an increasing number of layers. Figure 7 shows typical experimental curves of SBS load vs. deflection for specimens with 22 and 30 plies. The composites have non-planar interlaminar regions due to the presence of woven fabrics and therefore can experience a variety of different damage modes before interlaminar shear failure occurs under SBS loading. Most of the specimens exhibited the curves reported in Figure 7, where load rises gradually and then drops suddenly showing a distinct failure load developed in the sample, which is a behaviour generally ascribed to interlaminar shear failures.²⁸ It is also worth mentioning the comparison of these data with the ones available in the literature.²⁹ The measured ILSS values are comparable if not higher than those obtained by Lopresto et al. (~40 MPa),³ Kuzmin et al. (<50 MPa),²⁵ Varley et al. (~50–53 MPa),³⁰ Lee et al. (<50 MPa),³¹ Scalici et al. (~20 MPa)³² and many others.^{33–35} Therefore, the results of the present investigation can be correlated with the finding that the samples do not show poorly impregnated zones (dry regions or voids) and that the fibre/matrix adhesion quality is good.

Impact properties

The load–displacement curve represents the starting point to study the impact behaviour of composite

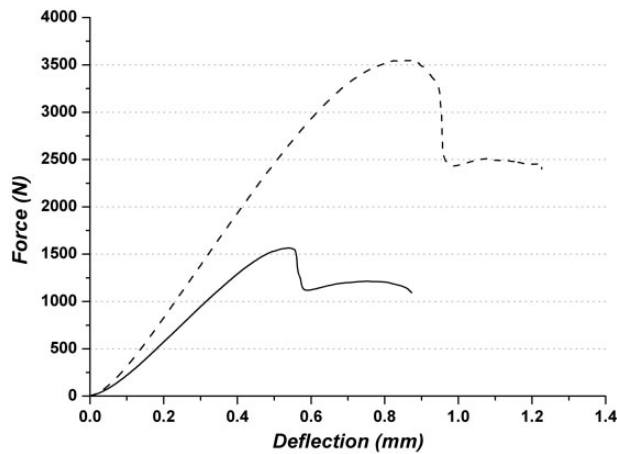


Figure 7. Typical force vs. displacement curves for short beam shear specimens with 22 (-) and 30 plies (-).

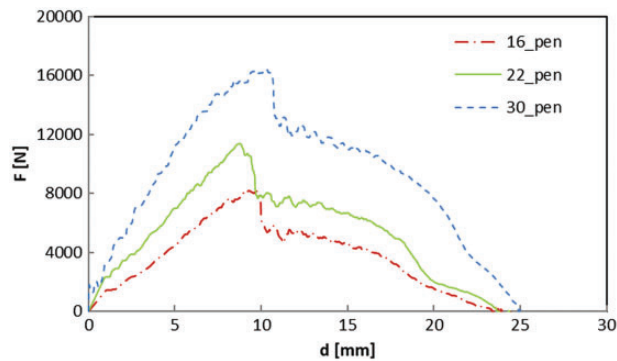


Figure 8. Load–displacement curves at penetration: comparison between the different thicknesses.

laminates. From this curve, it is possible to obtain useful information about the response of the material under dynamic loading. Figure 8 reports a comparison between the load–displacement curves at penetration for the three different tested thicknesses. As it is clear and expected, an increase of initial rigidity and maximum load is observed as the number of layers increases. It is worth noting that the first important load drop occurs in correspondence of the maximum load, while, in the case of ordinary carbon and glass fibre laminates, a significant load drop, denoting delamination onset and propagation,¹³ is observed well before the maximum load. This result means that the damage mechanisms are different from those of traditional laminates, where the delamination starts and propagates than the fibre failure. In this case, significant delamination starts together with the fibre failure and, as shown in Figure 9, seems to be localised under the material–impactor contact point.

The fractographic analysis, shown in Figure 10, allows noticing a concentration of the delamination under the impactor–material contact point between layers on the opposite side concerning the impacted one.

In Figures 11, 12 and 13, the typical curves obtained for basalt fibre laminates at increasing energy levels are reported. Figures clearly show that for the different energy levels, a closed type curve is always obtained. The samples are not penetrated/perforated by the impactor that rebounds and the area enclosed in the loop of the loading/unloading part of the curve is just the energy absorbed by deformation of the laminate and by irreversible damage.

As expected, the maximum impact load, F_{max} , increases as the impact energy, U , increases (Figure 14). Furthermore, the absorbed energy, U_a , increases as impact energy, U , increases (Figure 15) meaning that the effect of the increasing energies is

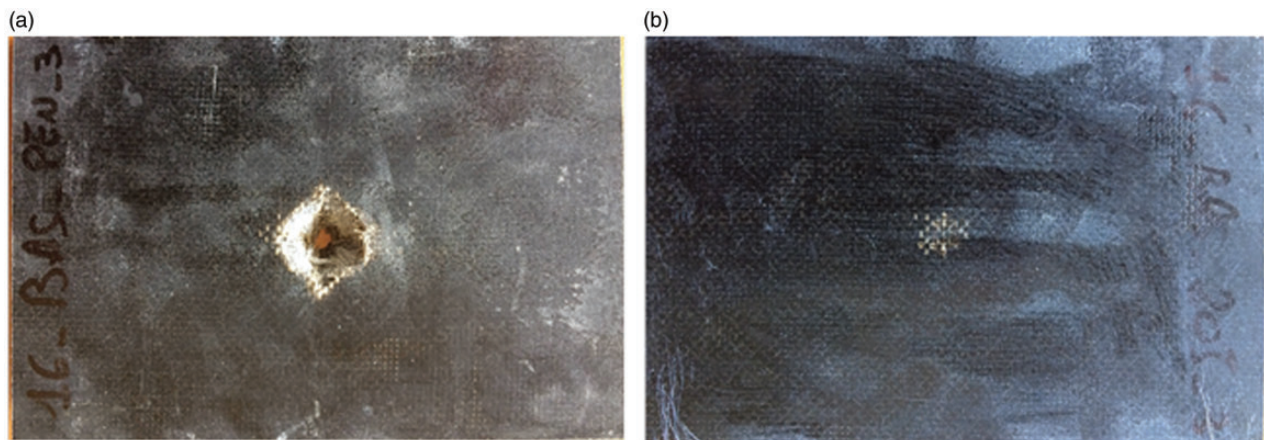


Figure 9. Visual inspections of impacted specimens, 16 layers: (a) penetration and (b) 20].

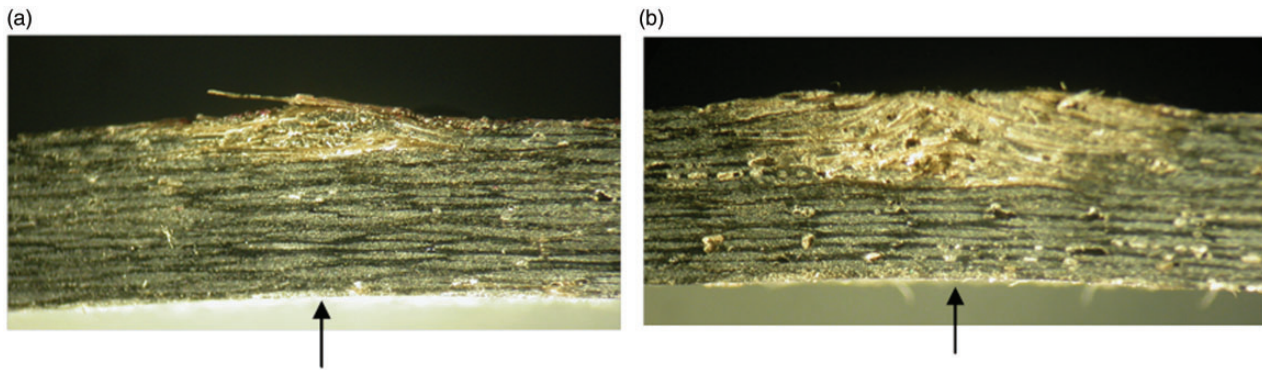


Figure 10. Fractographic analysis at 20 J (a) and 30 J (b) on 16-layer laminates. Arrows: impacted side.

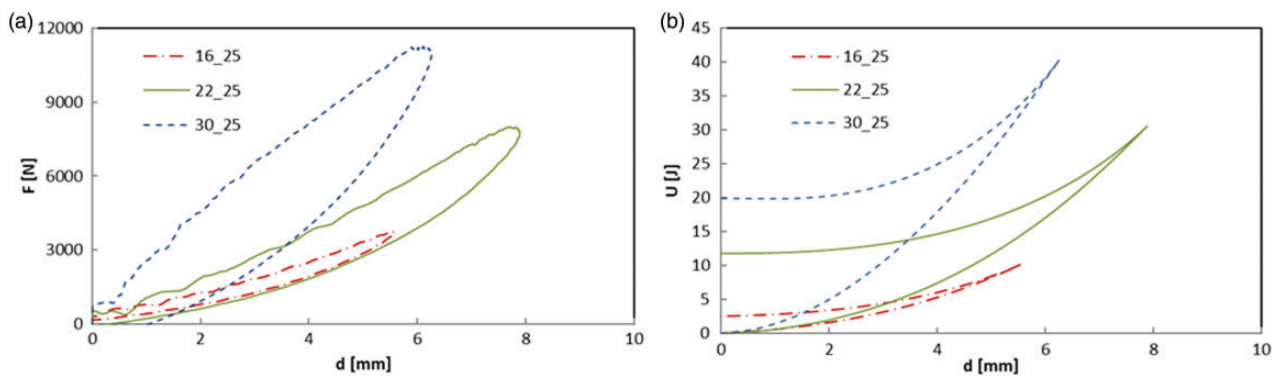


Figure 11. Impact curves for 16-, 22-, 30-layer laminates impacted at $U = 25\%$: (a) Force, F and (b) absorbed Energy, U_a .

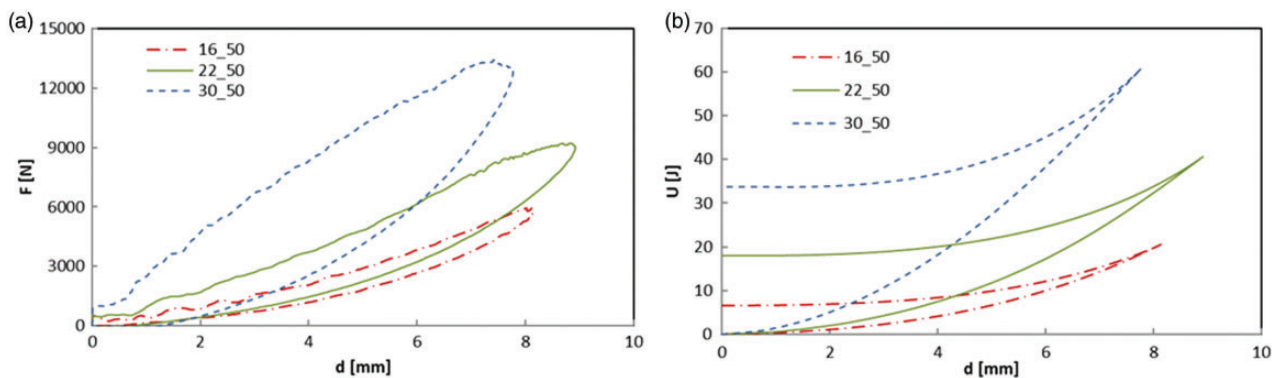


Figure 12. Impact curves for 16-, 22-, 30-layer laminates impacted at $U = 50\%$: (a) Force, F and (b) absorbed Energy, U_a .

like the increase in rigidity that causes an increase in internal damage.

In Figure 16, the maximum contact force (F_{\max}) is plotted as a function of the sample thickness (t) for all examined test samples. An entirely satisfactory correlation between the peak force and sample thickness for all impact energies was recorded, and the trend is well described by a power law $F = ax^i$ with a coefficient $R = 0.99$, $a = 1774 \text{ N/mm}$ and $i = 1.27$. The exponent,

i , is very close to the 1 of the Hertzian contact law, denoting the validity of the law in predicting the first failure load, already verified in the literature,¹³ confirming here the coincidence of the first failure load and the maximum peak.

A large amount of energy is required to penetrate the laminate with higher thickness, as clearly seen in Figure 17. This behaviour is supported by the validation of the Hertz contact law^{34,35} as it is possible to

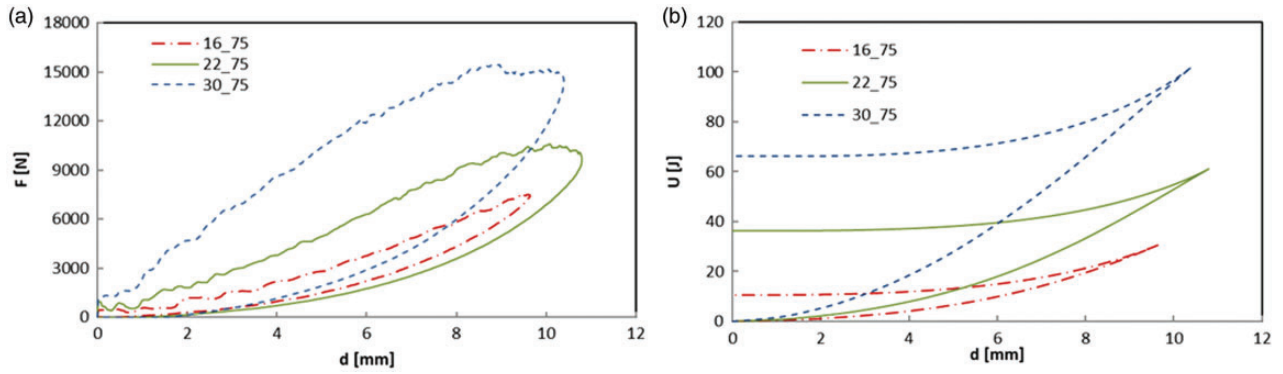


Figure 13. Impact curves for 16-, 22-, 30-layer laminates impacted at $U = 75\%$: (a) Force, F and (b) absorbed Energy, U_a .

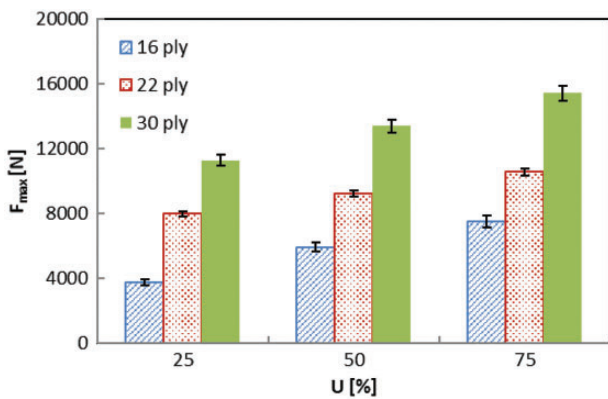


Figure 14. Maximum load, F_{max} , vs. impact energy, U .

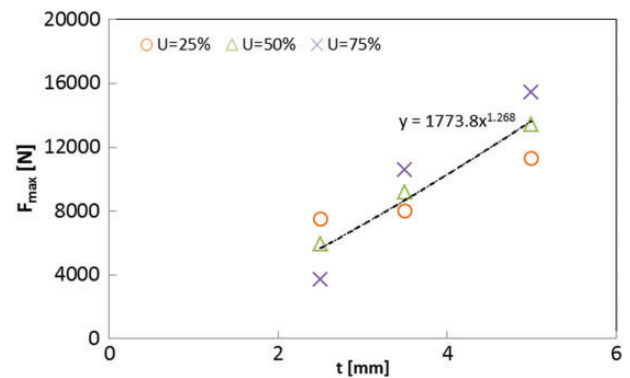


Figure 16. Maximum contact force vs. sample thickness for all investigated test energies.

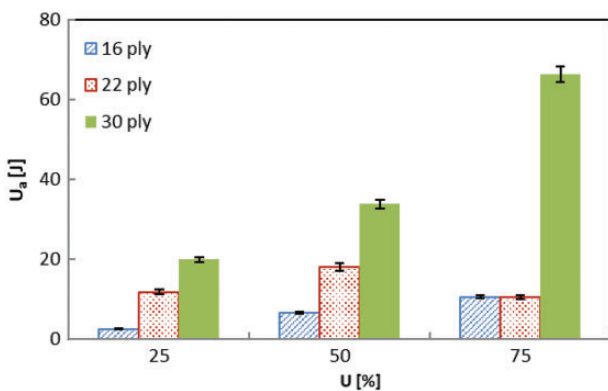


Figure 15. Absorbed energy, U_a , vs. impact energy, U .

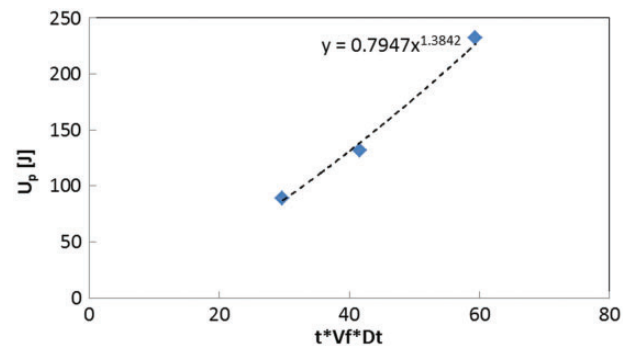


Figure 17. Penetration energy vs. the product $t \times V_f \times D_t$ for all investigated test thicknesses.

see in Figure 16. A good correlation between the penetration energy, U_p , and the product $t \times V_f \times D_t$, where t is the sample thickness, V_f the fibre volume fraction and D_t the penetrator diameter, was observed (see Figure 17). This power law has been developed to compare different data on the penetration energy of composite laminates and accounts for several both internal and external factors affecting the materials

energy-absorbing capacity. It resulted to be very useful to predict the penetration energy (U_p)^{37–39} and to establish that the main factors affecting the penetration energy are the total fibre thickness and the impactor diameter, whereas parameters as the resin type and content, reinforcement architecture, laminate stacking sequence, fibre orientations play a secondary role on the energy-absorption capacity. Thus, the parameter

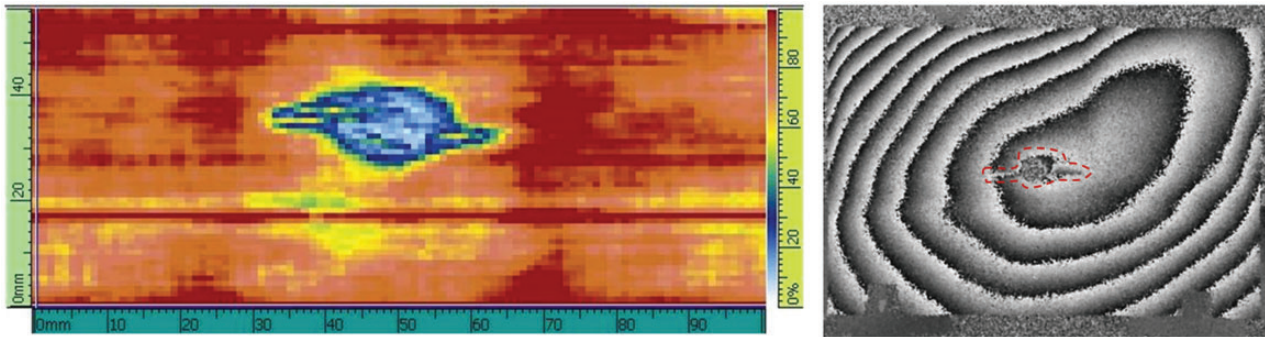


Figure 18. US C-scan and ESPI acquisition comparison. 16 plies, 20J.

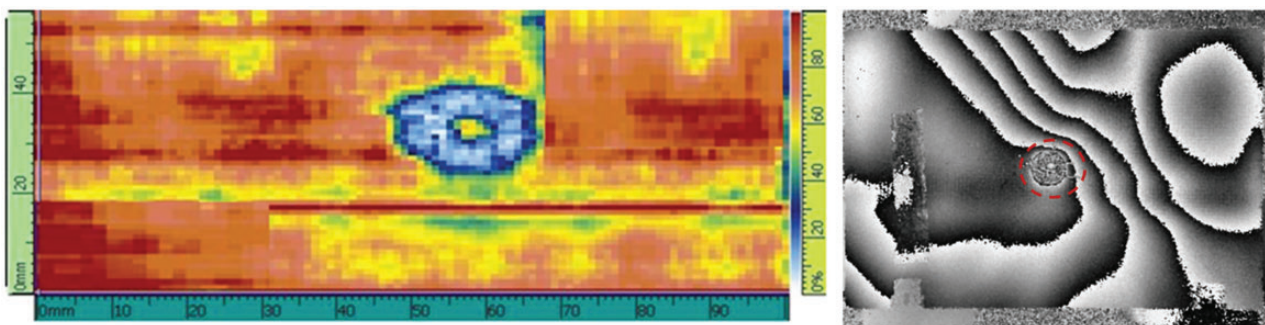


Figure 19. US C-scan and ESPI acquisition comparison. 22 plies, 20J.

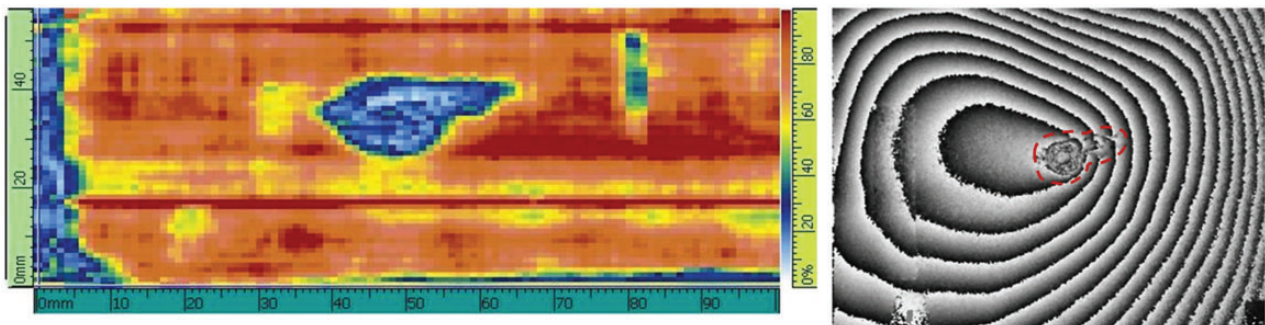


Figure 20. US C-scan and ESPI acquisition comparison. 30 plies, 20J.

actually influencing the penetration energy was found to be the product of $(t \times V_f \times D_i)$, and the relationship correlating the penetration energy to $(t \times V_f \times D_i)$ was found to be a power law⁴⁰ in which the exponent is a constant not depending on the particular material considered. This yielded a powerful tool to compare impact results obtained under different impact conditions and should allow the comparison of different materials by a single parameter. However, the exponent was found to change when the thickness of the laminates increased up to a specific value.⁴⁰

Delamination

The internal damage has been investigated by two different NDTs: the most used US technique⁴¹ and the ESPI. The internal damage seems to be confined around the impact point as visible in Figures 18, 19 and 20 that, for the same impact energy, $U = 50\%U_p$, and all thicknesses compare the damage images acquired by both US and ESPI techniques. A good correlation is noted for the damage shape obtained by the C-scan acquisition and the ESPI one, evidenced by

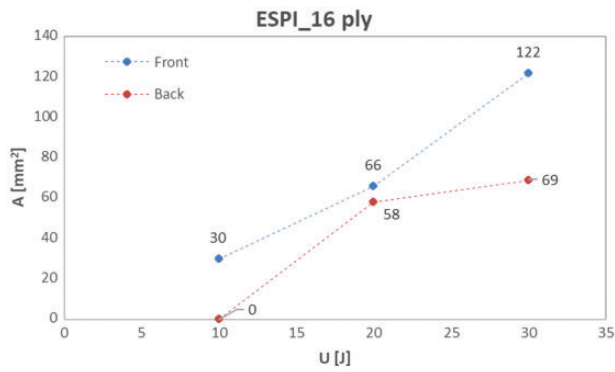


Figure 21. ESPI delaminated area, A , versus impact energy, U : comparison between front and back side; 16 plies.

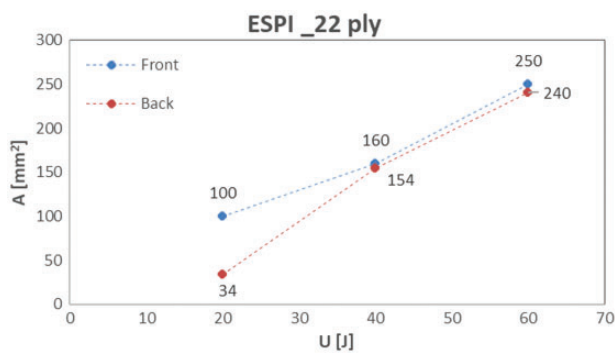


Figure 22. ESPI delaminated area, A , versus impact energy, U : comparison between front and back side; 22 plies.

a dashed red line. Of course, to obtain reliable results from the US, it was necessary to set the apparatus carefully to take into account the absorption coefficient of the signal, that depends on the fibre and matrix type, fibre orientation, thickness and composite stacking sequence. In the case of ESPI, being a full-field optical technique, no additional measurements were required.

To get information about the impact damage through the thickness of the laminates and exploit the characteristics of the speckle analysis, the ESPI technique was used to analyse both the front side and the back side of the plates (Figures 21–23). In particular, Figures 21 and 22 show the delaminated area of the front and back side as a function of the impact energy, obtained by ESPI in the case of laminates made with 16 and 22 plies. It can be noticed that in the case of lower impact energies the delaminated area for the composite with 16 plies, estimated on the back-side, is smaller respect to that on the front one. On the other hand, for impact energy greater than 40J, the composite with 22 plies is characterised by similar values of the front, and back side delaminated areas denoting that the impact energy has been distributed through the whole thickness.

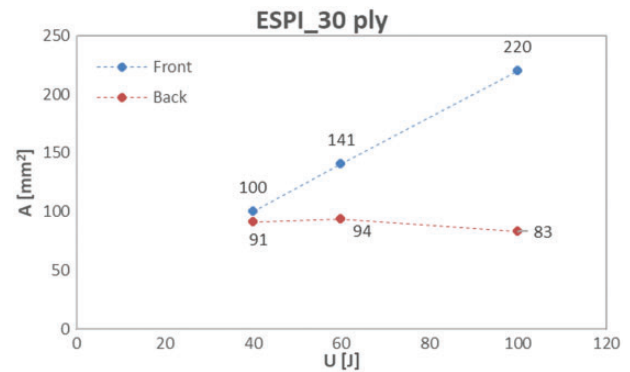


Figure 23. ESPI delaminated area, A , versus impact energy, U : comparison between front and back side; 30 plies.

The data for 30 plies composite are shown in Figure 23. In such case, the damages on the back side seem to be nearly constant denoting, as expected, that a thicker composite is more able to absorb the impact damage.

Table 2 reports the average values of the damaged area, A , that is estimated for all impacted specimens on the front sides at different impact energies by both NDTs. The delaminated areas recorded by ultrasonic analysis appear to be higher than those evaluated by the ESPI technique for the maximum and minimum thickness (16 and 30 plies). This result can be explained taking into account the characteristics of the investigated laminates or rather their low deformability that makes more difficult the measurements with ESPI especially on the edge of the impacted area. In general, the cross-ply composites are characterised not only by fibre breaking but also by matrix cracking on the impacted surface that is more difficult to be detected by ESPI technique, while US technique can detect the visible impact damage such as matrix cracking and subsurface delamination.

The measurements with the two different techniques are better highlighted in Figures 24 to 26, which correlate the delaminated area A and the impact energy, U : a similar evolution is observed for the results obtained by the ultrasonic analysis, US, and the innovative ESPI technique.

In particular, the delaminated area increases as the impact energy increases for all tested thicknesses (Figures 24–26). However, as the impact energy increases, a higher indentation depth is evaluated (Table 2). Then, as the thickness increases, the damage mechanism changes: the composite sample behaves like a stiffer material and the absorbed energy is distributed differently determining the damage and its propagation through different ways. Reminding that the indentation depth, I , is the footprint impress by the impactor on the impacted surface of the specimen (plastic deformation),³⁶ from Table 2 it is possible to note that the

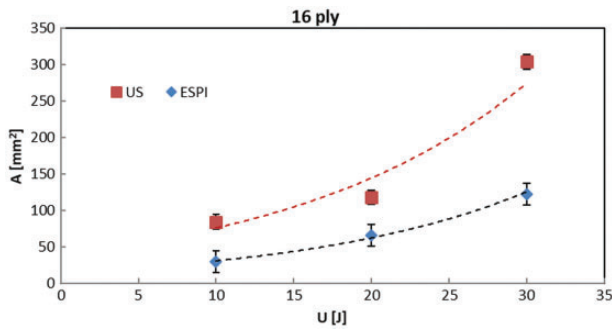


Figure 24. Delaminated area, A, vs. impact energy, U: comparison between US and ESPI technique; 16 plies.

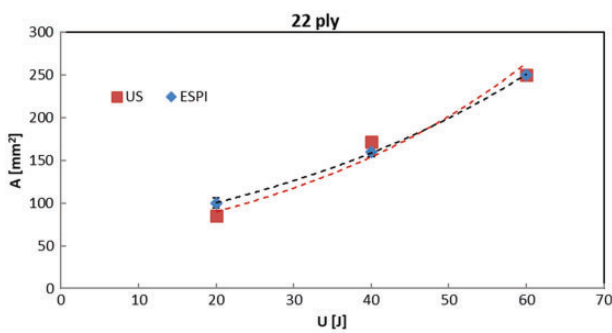


Figure 25. Delaminated area, A, vs. impact energy, U: comparison between US and ESPI technique; 22 plies.

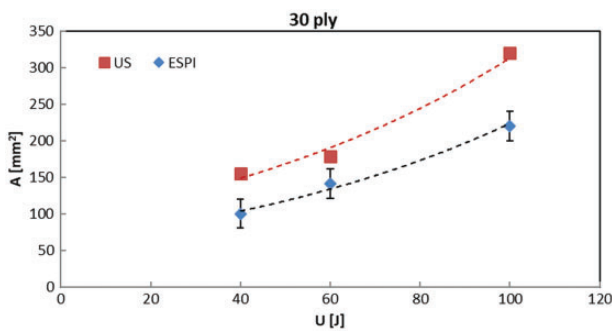


Figure 26. Delaminated area, A, vs. impact energy, U: comparison between US and ESPI technique; 30 plies.

composite with 30 plies, being more rigid, absorb the impact energy by a higher delamination and lower indentation respect to the composite with 22 plies. Further, for this latter laminate, the results of the two techniques are in agreement denoting a balance of the absorbed energy between the indentation and delamination spread. Finally, it is interesting to note that, for both NDTs, the correlation of the delaminated area, A, versus the maximum load, F_{max} , is a single linear curve for each thickness (Figures 27–29) that converges to the same intercept (F_{max} value) for zero delamination. This result

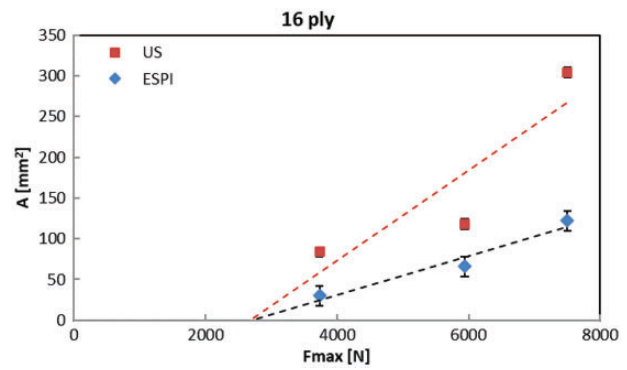


Figure 27. Delaminated area, A, vs. maximum load, F_{max} : comparison between US and ESPI technique; 16 plies.

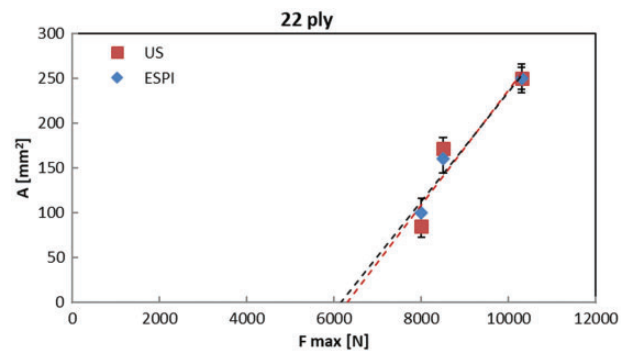


Figure 28. Delaminated area, A, vs. maximum load, F_{max} : comparison between US and ESPI technique; 22 plies.

Table 2. Delaminated area measurements.

16 Plies				22 Plies				30 Plies				
U [%]	A_{US} [mm ²]	A_{ESPI} [mm ²]	l [μm]	F_{max} [N]	A_{US} [mm ²]	A_{ESPI} [mm ²]	l [μm]	F_{max} [N]	A_{US} [mm ²]	A_{ESPI} [mm ²]	l [μm]	F_{max} [N]
25	84.1	30	86	3737	85	100	146	8000	155	100	64	11800
50	118	66	97	5942	172	160	272	8500	179	141	337	13500
75	304	122	112	7504	250	250	907	10300	320	220	506	15850

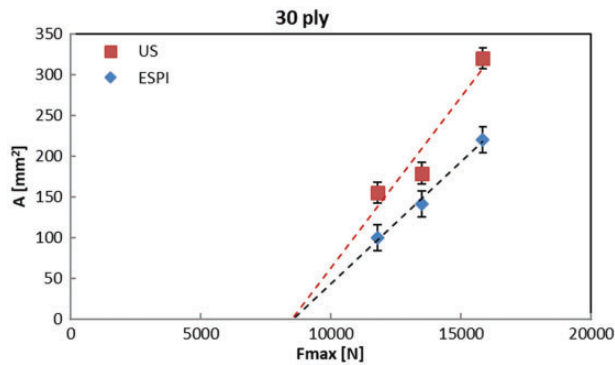


Figure 29. Delaminated area, A , vs. maximum load, F_{max} : comparison between US and ESPI technique; 30 plies.

is quite interesting and potentially useful, giving the possibility to know, for each thickness, the maximum load which delamination can be measured with both techniques. In particular, these limit values have been found equal to 2800, 6300 and 8700 N respectively for 16, 22 and 30 plies composites.

Conclusion

Epoxy fibre-reinforced basalt composites have been realised by vacuum infusion process by stacking 16, 22 and 30 fabric layers to obtain different thicknesses and to investigate the effect of this parameter on the mechanical properties and the impact behaviour. The manufactured composites were characterised by high and constant fibre volume fraction and good fibre impregnation as confirmed by the morphological analysis. This finding was also supported by the results of the mechanical results that evidenced a limited dispersion and negligible differences as a function of number of layers and thickness. The values of measured ILSS, tensile and flexural properties compared quite favourably with literature data.

The low-velocity impact tests highlighted a different behaviour of the basalt composites respect to conventional glass or carbon composites that start to delaminate before fibre failure. However, in this case, the delamination onset and propagation were observed in correspondence of the maximum load and was mainly concentrated under the impactor-material contact point. A large amount of energy was required to penetrate the laminate as the thickness increases, and this behaviour was confirmed by the validation of the Hertz contact law. Further, from the impact tests, an increase of initial rigidity and maximum load was observed as the number of layers increases. Finally, two NDTs, US and ESPI, were employed to estimate the delaminated area as a function of the impact energy and confirmed the results of the impact tests.

The damage shape, obtained by the NDT techniques, resulted quite similar validating both methods to analyse the impact damage. A similar correlation of the delaminated area A as a function of the impact energy, U was found and, in the case of the composite with 22 plies, the results of the two techniques were entirely in agreement denoting a balance of the absorbed energy between the indentation and delamination spread. Finally, a linear relationship was evidenced between the delaminated area, A and the maximum load, F_{max} , that converges to the same value for zero delamination. This result is quite interesting and potentially useful, giving the possibility to know, for each thickness, the maximum load beyond which delamination can be measured for both techniques.

Declaration of Conflicting Interests


The author(s) declared no potential conflicts of interest with respect to the research, authorship, and/or publication of this article.

Funding

The author(s) received no financial support for the research, authorship, and/or publication of this article.

ORCID iDs

I Papa  <https://orcid.org/0000-0002-5711-8822>

V Antonucci  <https://orcid.org/0000-0002-5708-7456>

References

1. Fiore V, Scalici T, Di Bella G, et al. A review on basalt fibre and its composites. *Compos Part B Eng* 2015; 74: 74–94.
2. Pickering KL, Aruan Efendy MG and Le TM. A review of recent developments in natural fibre composites and their mechanical performance. *Compos Part A Appl Sci Manuf* 2016; 83: 98–112.
3. Lopresto V, Leone C and De Iorio I. Mechanical characterisation of basalt fibre reinforced plastic. *Compos Part B Eng* 2011; 42: 717–723.
4. Singh H, Namala KK and Mahajan P. A damage evolution study of E-glass/epoxy composite under low velocity impact. *Compos Part B Eng* 2015; 76: 235–248.
5. Ricciardi MR, Papa I, Langella A, et al. Mechanical properties of glass fibre composites based on nitrile rubber toughened modified epoxy resin. *Compos Part B Eng* 2018; 139: 259–267.
6. Dorigato A and Pegoretti A. Fatigue resistance of basalt fibers-reinforced laminates. *J Compos Mater* 2012; 46: 1773–1785.
7. Liu Q, Shaw MT, Parnas RS, et al. Investigation of basalt fiber composite mechanical properties for applications in transportation. *Polym Compos* 2006; 27: 41–48.
8. Carmisciano S, De Rosa IM, Sarasini F, et al. Basalt woven fiber reinforced vinyl ester composites: flexural and electrical properties. *Mater Des* 2011; 32: 337–342.

9. Colombo C, Vergani L and Burman M. Static and fatigue characterisation of new basalt fibre reinforced composites. *Compos Struct* 2012; 94: 1165–1174. (<http://www.sciencedirect.com/science/article/pii/S0263822311003709> (accessed 17 September 2013)).
10. Sarasini F, Tirillò J, Valente M, et al. Effect of basalt fiber hybridization on the impact behavior under low impact velocity of glass/basalt woven fabric/epoxy resin composites. *Compos Part A Appl Sci Manuf* 2013; 47: 109–123.
11. Tehrani Dehkordi M, Nosrati H, Shokrieh MM, et al. The influence of hybridization on impact damage behavior and residual compression strength of intraply basalt/nylon hybrid composites. *Mater Des* 2013; 43: 283–290.
12. Sarasini F, Tirillò J, Valente M, et al. Hybrid composites based on aramid and basalt woven fabrics: impact damage modes and residual flexural properties. *Mater Des* 2013; 49: 290–302.
13. Caprino G, Lopresto V, Scarponi C, et al. Influence of material thickness on the response of carbon-fabric/epoxy panels to low velocity impact. *Compos Sci Technol* 1999; 59: 2279–2286.
14. Hosur MV, Murthy CRL, Ramamurthy TS, et al. Estimation of impact-induced damage in CFRP laminates through ultrasonic imaging. *NDT E Int* 1998; 31: 359–374.
15. Shang HM, Lim EM and Lim KB. Estimation of size and depth of debonds in laminates from holographic interferometry. *J Eng Mater Technol* 1992; 114: 127.
16. Grédiac M. The use of full-field measurement methods in composite material characterization: interest and limitations. *Compos Part A Appl Sci Manuf* 2004; 35: 751–761.
17. Jones R and Wykes C. *Holographic and speckle interferometry*. Cambridge: Cambridge University Press, 1989.
18. Ambu R, Aymerich F, Ginesu F, et al. Assessment of NDT interferometric techniques for impact damage detection in composite laminates. *Compos Sci Technol* 2006; 66: 199–205.
19. Papa I, Ricciardi MR, Antonucci V, et al. Impact behaviour of hybrid basalt/flax twill laminates. *Compos Part B Eng* 2018; 153: 17–25.
20. Busse G. Optoacoustic phase angle measurement for probing a metal. *Appl Phys Lett* 1979; 35: 759–760.
21. Antonucci V, Caputo F, Ferraro P, et al. Low velocity impact response of carbon fiber laminates fabricated by pulsed infusion: a review of damage investigation and semi-empirical models validation. *J Prog Aerospace Sci* 2016; 81: 26–40.
22. Pagliarulo V, Rocco A, Langella A, et al. Impact damage investigation on composite laminates: comparison among different NDT methods and numerical simulation. *Measur Sci Technol* 2015; 26: 085603.
23. Pagliarulo V, Palumbo R, Rocco A, et al. Evaluation of delaminated area of polymer/carbon nanotubes fiber reinforced composites after flexural tests by ESPI. *Proceedings of 2014 IEEE metrology for aerospace (MetroAeroSpace 2014)*, pp. 211–215, 29–30, 2014, Benevento, Italy ISBN 9781479920716.
24. Pagliarulo V, Farroni F, Ferraro P, et al. Combining ESPI with laser scanning for 3D characterization of racing tyres sections. *Opt Lasers Eng* 2018; 104: 71–77.
25. Kuzmin KL, Timoshkin IA, Gutnikov SI, et al. Effect of silane/nano-silica on the mechanical properties of basalt fiber reinforced epoxy composites. *Compos Interf* 2017; 24: 13–34.
26. Liu Q, Shaw MT, Parnas RS, et al. Investigation of basalt fiber composite aging behavior for applications in transportation. *Polym Compos* 2006; 27: 475–483.
27. Rosselli F and Santare MH. Comparison of the short beam shear (SBS) and interlaminar shear device (ISD) tests. *Compos Part A Appl Sci Manuf* 1997; 28: 587–594.
28. Abali F, Pora A and Shivakumar K. Modified short beam shear test for measurement of interlaminar shear strength of composites. *J Compos Mater* 2003; 37: 453–464.
29. Fan Z, Santare MH and Advani SG. Interlaminar shear strength of glass fiber reinforced epoxy composites enhanced with multi-walled carbon nanotubes. *Compos Part A Appl Sci Manuf* 2008; 39: 540–554.
30. Varley RJ, Tian W, Leong KH, et al. The effect of surface treatments on the mechanical properties of basalt-reinforced epoxy composites. *Polym Compos* 2013; 34: 320–329.
31. Lee S-O, Rhee KY and Park S-J. Influence of chemical surface treatment of basalt fibers on interlaminar shear strength and fracture toughness of epoxy-based composites. *J Ind Eng Chem* 2015; 32: 153–156.
32. Scalici T, Pitarresi G, Badagliacco D, et al. Mechanical properties of basalt fiber reinforced composites manufactured with different vacuum assisted impregnation techniques. *Compos Part B Eng* 2016; 104: 35–43.
33. Wang X, Zhao X, Wu Z, et al. Interlaminar shear behavior of basalt FRP and hybrid FRP laminates. *J Compos Mater* 2016; 50: 1073–1084.
34. Lee S-O, Choi S-H, Kwon SH, et al. Modification of surface functionality of multi-walled carbon nanotubes on fracture toughness of basalt fiber-reinforced composites. *Compos Part B Eng* 2015; 79: 47–52.
35. Chairman CA and Kumaresh Babu SP. Mechanical and abrasive wear behavior of glass and basalt fabric-reinforced epoxy composites. *J Appl Polym Sci* 2013; 130: 120–130.
36. Yang S and Sun C. Indentation law for composite laminates. In: *Compos. Mater. Test. Des.* (6th Conf., ASTM International, 100 Barr Harbor Drive, PO Box C700, West Conshohocken, PA 19428-2959, 1982, pp. 425–449. doi:10.1520/STP28494S.
37. Tan TM and Sun CT. Use of statical indentation laws in the impact analysis of laminated composite plates. *J Appl Mech* 1985; 52: 6.
38. Caprino G, Langella A and Lopresto V. Indentation and penetration of carbon fibre reinforced plastic laminates. *Compos Part B Eng* 2003; 34: 319–325.
39. Caprino G and Lopresto V. The significance of indentation in the inspection of carbon fibre-reinforced plastic

- panels damaged by low-velocity impact. *Compos Sci Technol* 2000; 60: 1003–1012.
40. Caprino G and Lopresto V. On the penetration energy for fibre-reinforced plastics under low-velocity impact conditions. *Compos Sci Technol* 2001; 61: 65–73.
41. Papa I, Lopresto V, Simeoli G, et al. Ultrasonic damage investigation on woven jute/poly (lactic acid) composites subjected to low velocity impact. *Compos Part B Eng* 2017; 115: 282–288.
42. Scarponi C and Valente M. An application of a new ultrasound technique to jute composite laminates subjected to low velocity impacts. *Int J Mater Product Technol* 2006; 26: 6–18.